

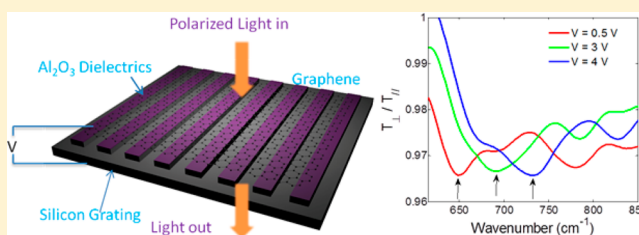
Excitation and Active Control of Propagating Surface Plasmon Polaritons in Graphene

Weilu Gao,[†] Gang Shi,[‡] Zehua Jin,^{†,§} Jie Shu,[†] Qi Zhang,[†] Robert Vajtai,[‡] Pulickel M. Ajayan,[‡] Junichiro Kono,^{†,§} and Qianfan Xu^{*,†}

[†]Department of Electrical and Computer Engineering, [‡]Department of Mechanical Engineering & Materials Science, and [§]Department of Physics and Astronomy, Rice University, Houston, Texas 77005, United States

ABSTRACT: We demonstrate the excitation and gate control of highly confined surface plasmon polaritons propagating through monolayer graphene using a silicon diffractive grating. The normal-incidence infrared transmission spectra exhibit pronounced dips due to guided-wave resonances, whose frequencies can be tuned over a range of $\sim 80 \text{ cm}^{-1}$ by applying a gate voltage. This novel structure provides a way to excite and actively control plasmonic waves in graphene and is thus an important building block of graphene plasmonic systems.

KEYWORDS: Active plasmonics, graphene surface plasmon polaritons, infrared optoelectronics, nanophotonics



The unique electronic properties of graphene^{1–3} make it a promising platform to build highly integrated active plasmonic devices^{4–7} and systems for a wide wavelength range from near-infrared to terahertz (THz),^{8–17} which enable manipulation and control of light confined in deeply subwavelength structures. Existing metal-based active plasmonic devices have either slow speeds¹⁸ or very limited tunability,^{4,19} and plasmonic devices based on a 2D electron gas in semiconductors²⁰ have been demonstrated only at cryogenic temperatures. In contrast, graphene has been shown to support surface plasmon polaritons (SPPs) with stronger mode confinement and lower propagation loss in the mid-infrared region due to its large carrier mobility at room temperature.^{9,21,22} The carrier density in graphene can be electrically adjusted dramatically with a small bias voltage applied to a field-effect transistor (FET), which can achieve tuning times below a nanosecond.²³ This unique combination makes graphene a promising material for electrically tunable active plasmonic devices.

The key challenge is to efficiently excite SPPs in graphene with an incident electromagnetic wave, given the large wavevector mismatch between the two waves. Recent studies demonstrated near-field excitations and observation of propagating SPPs in graphene using near-field microscopy with nanotips.^{21,22} This type of excitation has a low efficiency as only a very small percentage of incident photons can be converted to SPPs. In this paper, we experimentally demonstrate the excitation of SPPs in graphene using a silicon grating, where SPP is excited by a normal-incident free-space infrared wave through the guided-wave resonance (GWR).^{24–26} Besides assisting the optical excitations, the silicon grating also acts as a gate electrode to tune the resonance frequency of the device over a broad spectral range.

Results. To excite SPPs in graphene with a free-space infrared beam, their large difference in wavevector has to be overcome. Optical gratings are widely used to compensate for wavevector mismatches.^{20,27,28} Here we use a silicon diffractive grating underneath the graphene layer, as shown in Figure 1a, to facilitate the excitation. By compensating for the wavevector mismatch, a highly confined propagating SPP in graphene layer is excited by a normal-incidence free-space light beam through GWR.^{24,25}

Assuming that the conductivity of graphene follows the Drude model,^{9,29,30} the dispersion relationship of the transverse-magnetic (TM) mode SPP³¹ in a continuous monolayer of graphene is approximately given by⁹

$$\beta(\omega) \approx \frac{\pi \hbar^2 \epsilon_0 (\epsilon_{r1} + \epsilon_{r2})}{e^2 E_f} \left(1 + \frac{i}{\omega \tau} \right) \omega^2 \quad (1)$$

where $\beta(\omega)$ is the in-plane wavevector of the SPP, \hbar is the reduced Planck constant, ϵ_0 is the vacuum permittivity, ϵ_{r1} and ϵ_{r2} are the dielectric constants of the materials above and below the graphene film, τ is the carrier scattering time, $E_f = \hbar v_f (\pi n)^{1/2}$ is the Fermi energy measured from the Dirac point, n is the sheet carrier density, and $v_f \approx 10^6 \text{ m/s}$ is the Fermi velocity in graphene. The carrier scattering time τ determines the carrier mobility μ in graphene as $\tau = \mu E_f / e v_f^2$. The major component of the electric field of the SPP aligns with the wave propagation direction.

To compensate for the wavevector difference between the graphene SPPs and a free-space wave incident at an angle θ , the

Received: May 1, 2013

Revised: July 3, 2013

Published: July 29, 2013

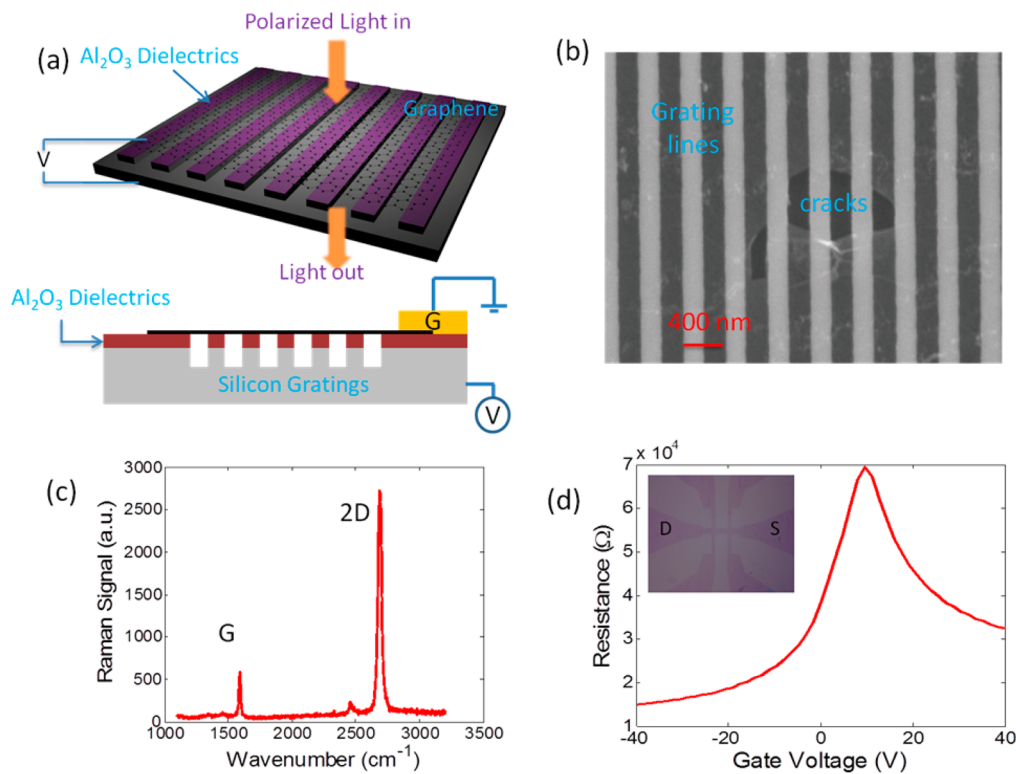


Figure 1. (a) Schematic of silicon-diffractive grating-assisted graphene plasmon excitation by guided-wave resonance (GWR). (b) Scanning electron microscopy (SEM) image of transferred graphene on a silicon grating with period $\Lambda = 400$ nm. A defective region is intentionally chosen here to show the contrast between graphene-covered and uncovered areas. (c) Raman spectrum of graphene transferred on a silicon grating indicated in part b. (d) The resistance of the graphene field effect transistor (FET) between the source (S) and the drain (D) as a function of gate voltage under vacuum (inset: graphene FET structure).

grating period Λ has to satisfy the following phase matching condition:

$$\text{Re}(\beta(\omega)) - \frac{\omega}{c} \sin \theta = \frac{2\pi}{\Lambda} \quad (2)$$

where c is the speed of light, θ is the incident angle from the sample normal, and ω is the angular frequency of the incident electromagnetic wave. Under a normal-incidence beam, the resonance frequency ω_0 of the GWR can be obtained from eqs 1 and 2 as:

$$\omega_0 = \sqrt{\frac{2e^2 E_f}{\hbar^2 \epsilon_0 (\epsilon_{r1} + \epsilon_{r2}) \Lambda}} \quad (3)$$

The resonance frequency ω_0 varies with E_f and Λ , which can be utilized to build active graphene plasmonic devices in different frequency regions.²⁶

To fabricate the structure shown in Figure 1a, periodically spaced trenches were etched into a lightly doped silicon substrate for grating formation (see Methods). The depth and length of each trench were ~ 250 nm and ~ 60 μm , respectively, and the grating period (Λ) varied from device to device. A 30-nm-thick layer of aluminum oxide was then deposited on top of the grating as the back-gating dielectric layer. Chemical vapor deposition (CVD)-grown monolayer graphene was then transferred on top of the grating as the propagation medium of SPPs. The strong mechanical property of graphene allowed the film to be suspended over the submicrometer-wide trenches, as shown in Figure 1b. The quality of graphene in the suspended regions was verified via Raman spectroscopy

(see Figure 1c). The locations of the G and 2D peaks (~ 1590 cm^{-1} and ~ 2688 cm^{-1} , respectively), the single Lorentzian shape of the 2D peak, the intensity ratio of the 2D to G peaks (>4.0), and the near absence of the D peak all indicate a high-quality monolayer of graphene after the transfer process.³² The inset of Figure 1d shows the structure of a graphene field effect transistor that was used to measure the mobility of the graphene. The main panel of Figure 1d shows the correlation between field-effect carrier transport and back-gating voltages, and the carrier mobility μ can be calculated from the linear regime of the transfer characteristics.³³ Most of the devices used in our experiments showed μ of ~ 1700 $\text{cm}^2 \cdot \text{V}^{-1} \cdot \text{s}^{-1}$.

We performed polarization-dependent transmission experiments on the fabricated devices using Fourier transform infrared spectroscopy (FTIR) in the mid-infrared (MIR) and far-infrared (FIR) regions, as schematically shown in Figure 2a (see also Methods).^{11,15,30} The phase-matching effect only occurs to SPPs propagating in the direction perpendicular to the grating lines, which is polarized in the same direction.²⁰ Therefore, SPPs can be excited only when the input light is polarized perpendicular to the grating lines, which introduces a dip in the transmission spectrum (T_{\perp}).²⁶ No resonance features are expected on the transmission spectra of light polarized along the grating lines (T_{\parallel}). Figure 2b shows the ratio T_{\perp}/T_{\parallel} as a function of frequency, which shows a resonant dip as light with the correct polarization couples incident radiation to the SPPs and its energy is absorbed in the graphene layer.²⁶

Figure 2b shows T_{\perp}/T_{\parallel} versus frequency for devices with different periods (Λ). For graphene on a bare silicon wafer, there is no observable difference in transmission between

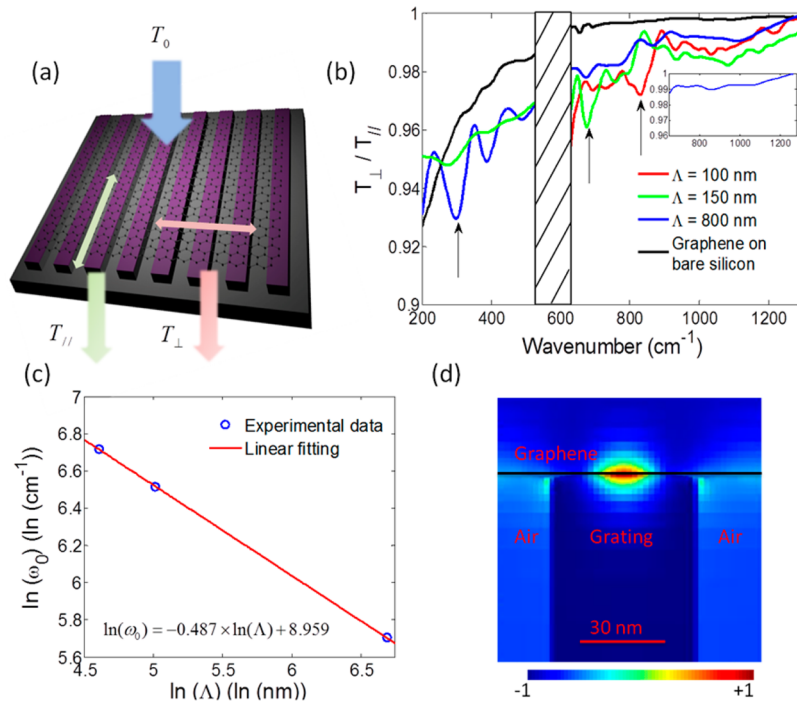


Figure 2. FTIR measurement results of the fabricated guided-wave resonance graphene plasmonic devices. (a) Schematics of the normal-incidence transmission measurement and the definitions of different polarizations for T_{\perp} and T_{\parallel} . (b) FTIR transmission spectra in the far-infrared (200–550 cm^{-1}) and mid-infrared (620–1300 cm^{-1}) for gratings with different periods. The arrows mark the positions of the resonances. The black line is the transmission of monolayer graphene normalized to the transmission of a bare silicon wafer. The shaded area represents the frequency region where the signal-to-noise ratio of detector was too low. Inset: The transmission spectrum of grating period $\Lambda = 800$ nm in mid-infrared region without graphene normalized to that of a bare silicon wafer. (c) The logarithm of resonance frequency ω_0 versus the logarithm of grating period Λ . Blue open circles correspond to the arrow positions in b and the red solid line is a linear fit with a fitted slope of -0.487 , which matches well with the theoretical prediction of -0.5 in eq 3. (d) Simulated mode profiles using the finite difference time domain (FDTD) method at the resonance frequency.

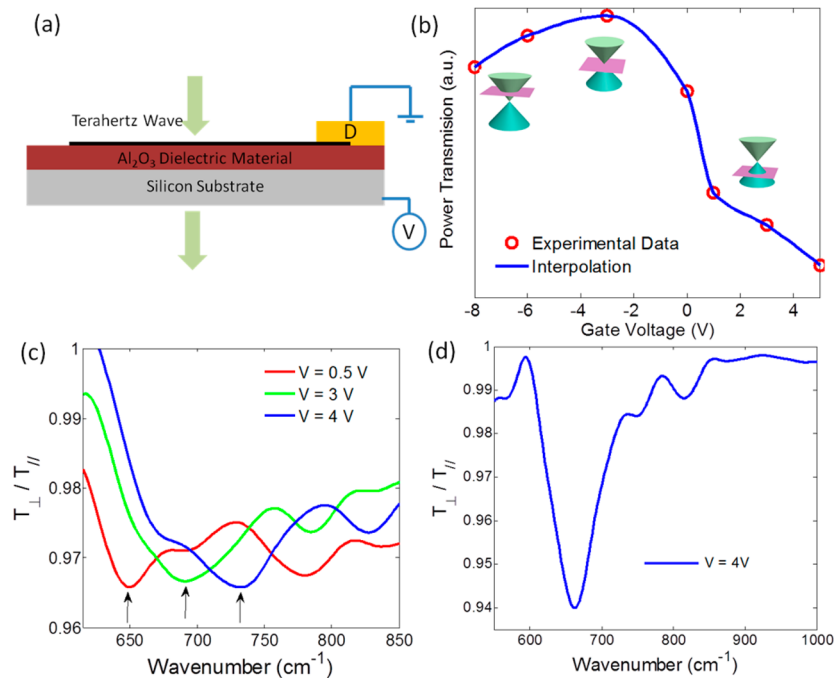


Figure 3. (a) Schematic of back-gate carrier density tuning in continuous graphene on an evaporated dielectric layer through THz-TDS measurements. (b) The total transmitted power of THz radiation changes with the gate voltage. The red dots are measurements, and the blue line is interpolation. (c) Electrical tuning of the fabricated GWR graphene plasmonic device with period $\Lambda = 100$ nm. Arrows indicate the position of the resonant dips. (d) The resonance of a GWR graphene plasmonic device with period $\Lambda = 200$ nm under 4-V bias, which has an extinction ratio ER $\sim 6\%$.

parallel and perpendicular polarized beams. However, all the other three devices with gratings exhibit transmission dips for light polarized perpendicular to the grating lines at particular frequencies and show no feature in other measured spectral range, indicating that the gratings play a key role in the SPP excitations. Figure 2c shows the relationship between the logarithm of resonance frequency ω_0 and the logarithm of grating period Λ , which fits well with eq 3. The spectrum position and extinction ratio (ER) can be fitted using finite difference time domain (FDTD) simulations with fitted Fermi level $E_f \sim 0.23$ eV and carrier mobility $\mu \sim 400$ cm²·V⁻¹·s⁻¹.²⁶ This Fermi level is comparable to the typical Fermi levels of graphene films transferred using similar methods, which are electrically measured to be between 0.2 and 0.3 eV while the carrier mobility is significantly lower than the DC mobility measured electrically on similar graphene material (~ 1700 cm²·V⁻¹·s⁻¹). Possible reasons for the reduction in mobility include nonuniformity in the grating structure due to imperfect fabrication, nonuniformity in the Fermi level in graphene,³⁴ and the many-body effects in graphene.^{35–37} The field distribution of SPPs was obtained through FDTD simulations as well. For a grating with period $\Lambda = 100$ nm, the calculated mode profile in the graphene layer is shown in Figure 2d, whose electric field intensity has a short decay length of ~ 20 nm in the vertical direction.

We used a back-gate structure to electrically control the carrier density and, thus, the resonance frequency of the device. A 30 nm aluminum oxide layer was deposited on the grating before graphene was transferred, and a voltage was applied between the substrate and graphene layer, as schematically shown in Figure 1a. The effectiveness of back-gate tuning was confirmed via terahertz time-domain spectroscopy (THz-TDS) by measuring broadband transmission at different applied voltages since the graphene intraband absorption changes with the position of the Fermi level E_f .³⁰ The schematic of this measurement is shown in Figure 3a. Figure 3b shows the spectrally integrated power of the transmitted THz beam versus gate voltage, demonstrating effective carrier density tuning in the graphene layer from the n-doped region to the p-doped region. The charge neutrality point is around -3 V, showing that graphene under zero bias is p-doped with a Fermi level E_f of ~ 0.26 eV (see Methods), which is close to what is estimated from the fitting with IR measurements (~ 0.23 eV).

Electrical tuning of the plasmon resonance is demonstrated in Figure 3c. Here T_{\perp}/T_{\parallel} is plotted versus frequency for different gate voltages in the mid-infrared region. As the gate voltage increases from 0.5 to 4 V, a large blue shift of ~ 80 cm⁻¹ of the resonance frequency is observed. Since the resonance frequency ω_0 of the unbiased structure is close to the lower frequency limit of our detector, we choose to apply only positive voltages to increase the doping level, which blue-shifts the center frequency²⁶ and moves the resonance farther away from the detector limit. The ER of the resonance varies from device to device, presumably due to sample uniformity variations. Figure 3d shows T_{\perp}/T_{\parallel} versus frequency for a device with the period $\Lambda = 200$ nm that has a higher ER of $\sim 6\%$. The ER of the resonance can be increased by improving the quality of the graphene layer and the fabrication processes.

In conclusion, we have demonstrated that subwavelength gratings can be utilized to excite propagating SPPs in graphene in the infrared wavelength region. This structure opens up new possibilities for building active plasmonic devices, ultrafast spatial light modulators with broad operation bandwidths,

graphene plasmonic sensors, and 2D plasmonic photonic circuits and metamaterials.

Methods. Gratings with different periods ranging from 100 to 800 nm are fabricated on a lightly doped silicon wafer (1–10 Ω ·cm) using standard electron beam lithography (JEOL-6500) with hydrogen silsesquioxane (HSQ) resist, which is followed by reactive ion etching (RIE) to etch away the silicon with ~ 250 nm depth. Buffered oxide etchant (BOE) is used to remove the top resist and passive oxide. Electron-beam evaporation is used to evaporate a thin (~ 30 nm) layer of aluminum oxide on the top of the silicon grating. The graphene layer is grown by chemical vapor deposition (CVD) on a copper foil and then transferred to the silicon grating using poly(methyl methacrylate) (PMMA) assisted wet-transfer techniques.^{38,39} Before the transfer process, a PMMA layer is spin-coated on graphene on the copper foil, and the copper foil is then etched away in a 10% nitric acid bath overnight. The PMMA-graphene film floating on the etchant is moved to distilled water several times to rinse the etchant residue and then scooped by the chip patterned with the grating structure.³⁹ The chip is dried in air overnight; then the PMMA layer is removed by acetone, and the whole chip is cleaned by isopropyl alcohol (IPA) carefully without damaging the graphene sheet.

The transmission spectra of devices in the mid-infrared region were taken using commercial JASCO FT/IR-660 Plus with a microscope and thalium bromoiodide (KRS₅) polarizer. Transmission for both polarizations was recorded, and their ratio T_{\perp}/T_{\parallel} is plotted. The far-infrared spectra were measured with unpolarized light and normalized to the transmission of a bare silicon wafer in a nitrogen gas purged chamber. Since far-infrared measurements require patterns of large size, the FIR spectrum of the 100-nm-period grating is not obtained due to fabrication limitations. Each measurement was repeated four times, and the results were averaged to produce the spectra in the paper. In our experiments, water vapor absorption in the mid-infrared region happens approximately 1300–2000 cm⁻¹ and carbon dioxide absorption mainly locates ~ 2350 cm⁻¹, which are out of the frequency range of our interest. From the featureless spectrum of the 800 nm period grating in the mid-infrared region in Figure 2c, we will see that the vapor and gas absorptions can be neglected.

The carrier concentration and Fermi level of graphene layer can be estimated using a parallel-plate capacitor model. The capacitor induced carrier concentration of graphene is $n = [(\epsilon_0 \epsilon_d V_g)/(ed)]$ and the Fermi level $E_f = \hbar v_f (\pi n)^{1/2}$. Here, the ϵ_d is the dielectric constant of the insulating layer, d is the thickness of the insulating layer, and V_g is the effective gate voltage measured from charge neutral point. Given the fast carrier diffusion⁴⁰ and the small grating period, we expect the carrier distribution in graphene to be nearly uniform even though the gate electrode is patterned. Assuming that $\epsilon_d = 9$ for aluminum oxide, $d = 30$ nm, and -3 V charge neutral point, the Fermi level of unbiased graphene is around 0.26 eV.

■ AUTHOR INFORMATION

Corresponding Author

*E-mail: qianfan@rice.edu.

Author Contributions

W.G. and G.S. contributed equally to this work.

Notes

The authors declare no competing financial interest.

■ ACKNOWLEDGMENTS

This work was partially supported by the Air Force Office of Scientific Research (AFOSR) Grant FA9550-12-1-0261 and the Department of Defense (DOD) grant W911NF-13-1-0140. J.K. acknowledges support from the National Science Foundation (through Grants No. OISE-0530220 and EEC-0540832), Department of Energy BES Program (through Grant No. DE-FG02-06ER46308), and the Robert A. Welch Foundation (through Grant No. C-1509). G.S., R.V. and P.M.A. acknowledge the support from STARnet, a Semiconductor Research Corporation program sponsored by MARCO and DARPA.

■ REFERENCES

- (1) Novoselov, K. S.; Geim, A. K.; Morozov, S. V.; Jiang, D.; Zhang, Y.; Dubonos, S. V.; Grigorieva, I. V.; Firsov, A. A. *Science* **2004**, *306* (5696), 666–9.
- (2) Geim, A. K.; Novoselov, K. S. *Nat. Mater.* **2007**, *6* (3), 183–91.
- (3) Castro Neto, A. H.; Guinea, F.; Peres, N. M. R.; Novoselov, K. S.; Geim, A. K. *Rev. Mod. Phys.* **2009**, *81* (1), 109–162.
- (4) MacDonald, K. F.; Samson, Z. L.; Stockman, M. I.; Zheludev, N. I. *Nat. Photonics* **2009**, *3* (1), 55–58.
- (5) Gjonaj, B.; Aulbach, J.; Johnson, P. M.; Mosk, A. P.; Kuipers, L.; Lagendijk, A. *Nat. Photonics* **2011**, *5* (6), 360–363.
- (6) Chen, H. T.; Padilla, W. J.; Zide, J. M. O.; Gossard, A. C.; Taylor, A. J.; Averitt, R. D. *Nature* **2006**, *444* (7119), 597–600.
- (7) Schuller, J. A.; Barnard, E. S.; Cai, W. S.; Jun, Y. C.; White, J. S.; Brongersma, M. L. *Nat. Mater.* **2010**, *9* (4), 193–204.
- (8) Rana, F. *IEEE Trans. Nanotechnol.* **2008**, *7* (1), 91–99.
- (9) Jablan, M.; Buljan, H.; Soljacic, M. *Phys. Rev. B* **2009**, *80* (24), 245435.
- (10) Bao, Q. L.; Zhang, H.; Wang, B.; Ni, Z. H.; Lim, C. H. Y. X.; Wang, Y.; Tang, D. Y.; Loh, K. P. *Nat. Photonics* **2011**, *5* (7), 411–415.
- (11) Ju, L.; Geng, B. S.; Horng, J.; Girit, C.; Martin, M.; Hao, Z.; Bechtel, H. A.; Liang, X. G.; Zettl, A.; Shen, Y. R.; Wang, F. *Nat. Nanotechnol.* **2011**, *6* (10), 630–634.
- (12) Koppens, F. H. L.; Chang, D. E.; de Abajo, F. J. G. *Nano Lett.* **2011**, *11* (8), 3370–3377.
- (13) Bao, Q. L.; Loh, K. P. *ACS Nano* **2012**, *6* (5), 3677–3694.
- (14) Grigorenko, A. N.; Polini, M.; Novoselov, K. S. *Nat. Photonics* **2012**, *6* (11), 749–758.
- (15) Yan, H. G.; Li, X. S.; Chandra, B.; Tulevski, G.; Wu, Y. Q.; Freitag, M.; Zhu, W. J.; Avouris, P.; Xia, F. N. *Nat. Nanotechnol.* **2012**, *7* (5), 330–334.
- (16) Yan, H. G.; Xia, F. N.; Li, Z. Q.; Avouris, P. *New J. Phys.* **2012**, *14*, 125001.
- (17) Fang, Z. Y.; Thongrattanasiri, S.; Schlather, A.; Liu, Z.; Ma, L. L.; Wang, Y. M.; Ajayan, P. M.; Nordlander, P.; Halas, N. J.; de Abajo, F. J. G. *ACS Nano* **2013**, *7* (3), 2388–2395.
- (18) Pala, R. A.; Shimizu, K. T.; Melosh, N. A.; Brongersma, M. L. *Nano Lett.* **2008**, *8* (5), 1506–1510.
- (19) Dionne, J. A.; Diest, K.; Sweatlock, L. A.; Atwater, H. A. *Nano Lett.* **2009**, *9* (2), 897–902.
- (20) Allen, S. J.; Tsui, D. C.; Logan, R. A. *Phys. Rev. Lett.* **1977**, *38* (17), 980–983.
- (21) Chen, J. N.; Badioli, M.; Alonso-Gonzalez, P.; Thongrattanasiri, S.; Huth, F.; Osmond, J.; Spasenovic, M.; Centeno, A.; Pesquera, A.; Godignon, P.; Elorza, A. Z.; Camara, N.; de Abajo, F. J. G.; Hillenbrand, R.; Koppens, F. H. L. *Nature* **2012**, *487* (7405), 77–81.
- (22) Fei, Z.; Rodin, A. S.; Andreev, G. O.; Bao, W.; McLeod, A. S.; Wagner, M.; Zhang, L. M.; Zhao, Z.; Thieme, M.; Dominguez, G.; Fogler, M. M.; Neto, A. H. C.; Lau, C. N.; Keilmann, F.; Basov, D. N. *Nature* **2012**, *487* (7405), 82–85.
- (23) Liu, M.; Yin, X. B.; Ulin-Avila, E.; Geng, B. S.; Zentgraf, T.; Ju, L.; Wang, F.; Zhang, X. *Nature* **2011**, *474* (7349), 64–67.
- (24) Rosenblatt, D.; Sharon, A.; Friesem, A. A. *IEEE J. Quantum Electron.* **1997**, *33* (11), 2038–2059.
- (25) Sharon, A.; Glasberg, S.; Rosenblatt, D.; Friesem, A. A. *J. Opt. Soc. Am. A* **1997**, *14* (3), 588–595.
- (26) Gao, W. L.; Shu, J.; Qiu, C. Y.; Xu, Q. F. *ACS Nano* **2012**, *6* (9), 7806–7813.
- (27) Elston, S. J.; Bryanbrown, G. P.; Sambles, J. R. *Phys. Rev. B* **1991**, *44* (12), 6393–6400.
- (28) Watts, R. A.; Preist, T. W.; Sambles, J. R. *Phys. Rev. Lett.* **1997**, *79* (20), 3978–3981.
- (29) Horng, J.; Chen, C. F.; Geng, B. S.; Girit, C.; Zhang, Y. B.; Hao, Z.; Bechtel, H. A.; Martin, M.; Zettl, A.; Crommie, M. F.; Shen, Y. R.; Wang, F. *Phys. Rev. B* **2011**, *83* (16), 165113.
- (30) Ren, L.; Zhang, Q.; Yao, J.; Sun, Z. Z.; Kaneko, R.; Yan, Z.; Nanot, S.; Jin, Z.; Kawayama, I.; Tonouchi, M.; Tour, J. M.; Kono, J. *Nano Lett.* **2012**, *12* (7), 3711–3715.
- (31) Jablan, M.; Buljan, H.; Soljacic, M. *Opt. Express* **2011**, *19* (12), 11236–11241.
- (32) Ferrari, A. C.; Meyer, J. C.; Scardaci, V.; Casiraghi, C.; Lazzeri, M.; Mauri, F.; Piscanec, S.; Jiang, D.; Novoselov, K. S.; Roth, S.; Geim, A. K. *Phys. Rev. Lett.* **2006**, *97* (18), 187401.
- (33) Schwierz, F. *Nat. Nanotechnol.* **2010**, *5* (7), 487–496.
- (34) Buron, J. D.; Petersen, D. H.; Boggild, P.; Cooke, D. G.; Hilke, M.; Sun, J.; Whiteway, E.; Nielsen, P. F.; Hansen, O.; Yurgens, A.; Jepsen, P. U. *Nano Lett.* **2012**, *12* (10), 5074–5081.
- (35) Li, Z. Q.; Henriksen, E. A.; Jiang, Z.; Hao, Z.; Martin, M. C.; Kim, P.; Stormer, H. L.; Basov, D. N. *Nat. Phys.* **2008**, *4* (7), 532–535.
- (36) Peres, N. M. R.; Ribeiro, R. M.; Neto, A. H. C. *Phys. Rev. Lett.* **2010**, *105* (5), 055501.
- (37) Tassin, P.; Koschny, T.; Kafesaki, M.; Soukoulis, C. M. *Nat. Photonics* **2012**, *6* (4), 259–264.
- (38) Li, X. S.; Cai, W. W.; An, J. H.; Kim, S.; Nah, J.; Yang, D. X.; Piner, R.; Velamakanni, A.; Jung, I.; Tutuc, E.; Banerjee, S. K.; Colombo, L.; Ruoff, R. S. *Science* **2009**, *324* (5932), 1312–1314.
- (39) Suk, J. W.; Kitt, A.; Magnuson, C. W.; Hao, Y. F.; Ahmed, S.; An, J. H.; Swan, A. K.; Goldberg, B. B.; Ruoff, R. S. *ACS Nano* **2011**, *5* (9), 6916–6924.
- (40) Ruzicka, B. A.; Wang, S.; Werake, L. K.; Weintrub, B.; Loh, K. P.; Zhao, H. *Phys. Rev. B* **2010**, *82* (19), 195414.